Received: 30 June 2023 | Revised: 17 October 2023 | Accepted: 27 October 2023

DOI: 10.1002/pip.3753

RESEARCH ARTICLE

PROGRESS IN PHOTOVOLTAICS WILEY

Outdoor measurements of a full-size bifacial Pero/Si tandem module under different spectral conditions

David Chojniak[1] | Marc Steiner[1] | Sebastian Kasimir Reichmuth[1,2] | Torsten Rößler[1] | Alexandra Schmid[1] | Gerald Siefer[1] | Stefan W. Glunz[1,2]

[1]Fraunhofer Institute for Solar Energy Systems ISE, Freiburg, Germany

[2]Chair for Photovoltaic Energy Conversion, Department of Sustainable Systems Engineering INATECH, University of Freiburg, Freiburg, Germany

Correspondence
David Chojniak, Fraunhofer Institute for Solar Energy Systems ISE, Heidenhofstr. 2, 79110 Freiburg, Germany.
Email: david.chojniak@ise.fraunhofer.de

Funding information
German Federal Ministry for Economic Affairs and Climate Action (BMWK), Grant/Award Number: 03EE1087B

[Correction added on 19 January 2024, after first online publication: The third author's name has been corrected from 'Kasimir Reichmuth' to 'Sebastian Kasimir Reichmuth' in this version.]

Abstract

In recent years, significant progress has been made in terms of efficiency and stability of perovskite on silicon (Pero/Si) tandem solar cells. Nevertheless, most of these activities are focused on small-area laboratory cells while the availability of large-area solar cells suitable for module integration on an industrial level remains limited, and therefore, measurements of tandem modules are rare. However, the reliable measurement of tandem modules is a prerequisite to evaluate the real potential of this rapidly developing technology for the photovoltaic market. In this study, we present the first published outdoor measurement of a full-size bifacial Pero/Si tandem solar cell module. Our focus is on analyzing the spectral influences on the outdoor performance of the device through a qualitative assessment of the modules *I*–*V* parameter conducted over the course of a measurement day. Based on continuous monitoring of the ambient and module conditions, we provide consistent explanations for the complex interplay between the incident irradiance on both the front and backside of the module, as well as the module temperature. Based on our findings, we finally discuss how to appropriately account for the influence of bifaciality in the case of bifacial tandem modules, where the procedures used for bifacial single-junction devices cannot be easily applied due to subcell limitation effects. Throughout the study, we present important insights into the real-world characteristics of a bifacial Pero/Si tandem model, discuss and explain various influences on the modules performance, and therefore provide crucial information for an optimal cell design for bifacial Pero/Si tandem devices.

KEYWORDS
bifacial tandem solar cell modules, component cells, outdoor measurements, perovskite–silicon tandem solar cell modules, photovoltaics

1 | INTRODUCTION

The perovskite silicon tandem technology is currently considered as promising candidate to undergo the levelized costs of electricity of the silicon single-junction technology,[1,2] which has dominated the solar industry for many years.[3] Perovskite materials are considered as ideal top cells for silicon-based tandem cells due to their low production cost,[1,4] as well as the remarkable optoelectronic properties[5] and

tunable bandgaps.[6] The potential of this material combination has been demonstrated with several efficiency records published by different research groups[7–11] within a rather short time period, leading to a current record efficiency of 33.7% on a 1 cm^2 dual-junction Pero/Si tandem solar cell.[10] In addition to the successful and fast development of small-area devices, the upscaling of Pero/Si tandems also became a main focus using the well-developed silicon solar cell technology as an efficient and economically viable "substrate" technology to enable module integration and push the technology towards market commercialization.[12] Currently, an efficiency of 28.6%[13] realized on a M4 Wafer (258.15 cm^2) sets the benchmark for large-area devices. However, even high laboratory efficiencies of single wafers are of secondary interest when it comes to a successful market entry. Whether or not this new technology can enter the market will be decided in large part based on its long-term levelized cost of electricity. This in turn is strongly connected to the performance of full modules under realistic outdoor conditions, which obviously differ significantly from the conditions at hand during indoor calibration under standard test conditions.[14]

While the tandem architecture offers many advantages that lead to the efficiency records mentioned above, there are also challenges arising from the combination of several subcells. Different outdoor measurement conditions such as the varying spectral irradiance[15] and temperature effects[16] can significantly change a tandem module's performance. This statement especially holds for tandem modules using a two-terminal cell architecture.[17] The series connection of the individual subcells of the tandem cells in these modules result in tandem effects affecting the *I*–*V* parameters in different ways.[15]

The additional complexity of such devices, when compared to silicon single-junction modules, does further increase if a bifacial architecture is used. Bifacial modules can not only use the frontside irradiance coming directly from the sun but also the rear-side irradiance reflected from the surrounding, potentially increasing the generated power per area of such devices.[18]

While outdoor measurements of individual cells or small modules have already been demonstrated by different groups,[16,19–21] the investigation of a full module has not been reported yet. In addition, previous publications have been primarily limited to the observation of the module's performances over time while deeper insights into the module's characteristic under different outdoor conditions have not been given. Yet, a deeper understanding of the influence of different outdoor conditions on the individual subcells and their interplay within a module is the key for accurate measurements as well as their interpretation, which can finally be translated into further improvements in the cell and module architecture. Merging the spectral sensitivity of tandem modules with the additional rear-side contribution of bifacial devices, different combined effects result, which are strongly affecting module characteristics determined during outdoor measurements.

To comprehensibly explain these effects occurring in outdoor measurements of a bifacial tandem module, we analyze the characteristics of a full-size Pero/Si tandem module exposed to outdoor measurement conditions over a full measurement day. In the first part of our work, we present the utilized measurement setup that allows for simultaneous recording of the *I*–*V* characteristics of the module and a comprehensive dataset of ambient measurement conditions. Focusing on the determination of the spectral conditions, we are making use of an outdoor measurement procedure which has been established at Fraunhofer ISE for the outdoor calibration of III–V multi-junction concentrator photovoltaic (CPV) modules for many years.[22–24] This procedure, which is based on the use of a component cell sensor (described in detail in Section 3), has lately been adapted for the outdoor rating of monofacial III–V tandem modules.[25] In this publication, we are for the first time demonstrating the applicability of this procedure for outdoor measurements of Pero/Si tandem modules.

In the second part of the paper, we show outdoor measurements carried out on the utilized Pero/Si tandem module. To accurately explain the different effects resulting from the combination of bifaciality and the series connection of the subcells, we are analyzing the characteristic of all *I*–*V* parameters measured during the measurement day in depth. Using the continuously measured outdoor conditions, we are able to give consistent explanations for the appearing effects in the module's operation, affecting the individual *I*–*V* parameters in different ways.

In the last part of this publication, we focus on the power generated by the investigated module which basically shows the interaction of the effects on all individual *I*–*V* parameters discussed beforehand. We are raising the question of how to correctly interpret the performance of a bifacial tandem module, especially when it comes to a comparison with monofacial modules. Since different irradiance definitions are used for the calculation of the module's efficiency in the case of monofacial and bifacial modules, care must be taken when comparing both technologies. This is especially true for bifacial tandem modules since the contribution of the rear-side irradiance cannot be defined as a constant "gain factor," translatable to a backside efficiency, as it is done for bifacial single-junction modules.[26]

2 | MEASUREMENT SETUP

The presented measurements are performed on a full-size bifacial Pero/Si tandem module with a total module area of 1.91 m^2. The investigated module is a prototype manufactured within a cooperation between Oxford PV and Fraunhofer ISE using M4 (161.7 cm^2) Pero/Si tandem solar cells. The module consists of 60 cells and is divided into two parallel connected strings with 30 cells in series, a module layout typically used for half-cut cells.[27] This interconnection concept doubles the current of the module while it bisects the voltage. Due to the tandem architecture with two series-connected subcells, this results in current and voltage values which are close to the ones a silicon single-junction module of the same size would provide. We would like to note that the cell and module design is still in a development status such that properties like the module area, connection design or the current balancing of top and bottom cell might still undergo changes for modules following this prototype. The presented module measurements were performed on a dual axis tracker on our outdoor measurement setup at Fraunhofer ISE in Freiburg, Germany (48.01° N, 7.83° E). The tracker follows the course of the sun such that the direct portion of the incident irradiance hits

the module perpendicular at any time. A photo of the module mounted on the dual axis tracker (a) and a schematic representation of the modules interconnection principle (b) are presented in Figure 1.

The *I*–*V* parameters of the module have been determined every 2 min using an electric load. The load is capable to operate in constant current, constant voltage, and constant resistance mode and enables *I*–*V* measurements in the fourth quadrant. By compensating the line resistances, the *I*–*V* curves can be recorded close to the short-circuit current (I_{SC}) of the module. Current and voltage values are recorded simultaneously.[28] Between the measurements of the *I*–*V* curves the module was kept at its maximum power point (MPP). Starting at the initial MPP voltage determined from the previous *I*–*V* scan, the voltage of the module is continuously readjusted in the direction of increasing power. All parameters presented in the results section of this publication are determined from *I*–*V* curves measured in forward scan direction with a sweep time of 5 s. A faster sweep time was considered as unsuitable due to transient effects of the perovskite top cells[29] while a slower sweep time could result in disturbed *I*–*V* curves due to continuously varying ambient conditions for example caused by moving clouds. A continuous measurement of forward and reverse *I*–*V* curves was not possible due to limitations of the measurement setup utilized. Different sensors were used to continuously monitor the ambient conditions the module was exposed to: a temperature sensor to track the ambient temperature, a wind sensor to measure the wind speed, and two calibrated pyranometers to determine the frontside and rear-side irradiance intensity on to the module. Additionally, a component cell sensor[23,30] was utilized to evaluate the spectral conditions present during each *I*–*V* measurement of the module. The working principle and applicability of these sensors will be discussed in more detail in the next section. The module temperature was assessed using a Pt100 temperature sensor encapsulated in silicone and fixed close to the center on the module's rear side.

3 | COMPONENT CELL SENSOR

Component cell sensors are well known and commonly used for the evaluation of outdoor spectral conditions in CPV applications and have been proofed to provide accurate and fast information about the outdoor spectral distribution.[30] The applied sensor set consists of three calibrated 4 cm^2 component cells representing the top, middle, and bottom cell of a $Ga_{0.50}In_{0.50}P/Ga_{0.99}In_{0.01}As/Ge$ triple-junction solar cell.[22,23] Component cells are single-junction solar cells, which are optically (absorption and transmission) equivalent to the whole multi-junction cell but electrically behaving as one of the multi-junction's subcells.[22] All three component cells are primarily sensitive in different spectral bands of the solar spectrum, only showing a small overlap in their external quantum efficiencies (EQEs). The bandgaps of the cells are selected in a way that the influences of atmospheric parameters, primarily defining the shape of the solar spectrum, are affecting the current of the component cells separately to some extent. Therefore, Component Cells 1 (absorption edge ~720 nm) and 2 (absorption edge ~930 nm) are primarily sensitive to changes in air mass (AM) and aerosol optical depth (AOD), while Cell 3 (absorption edge at ~ 1950 nm) is mainly affected by the amount of precipitable water (PW) in the atmosphere. To assess the outdoor spectral conditions, the currents of the cells, assessed using resistors that keep the cells close to their short-circuit conditions, are used to calculate spectral matching ratios (SMRs). For the CPV power rating, which has lately been adapted for flat-plate tandem modules, the SMRs between all three cells, SMR12, SMR13, and SMR23, are utilized.[25,31] However, for this publication, the germanium bottom cell is not considered to improve the readability of the presented graphs. Due to the spectral responsivity of the investigated tandem module which is limited by the absorption edge of the silicon bottom cell, located at approximately 1200 nm, this simplification is acceptable for the presented

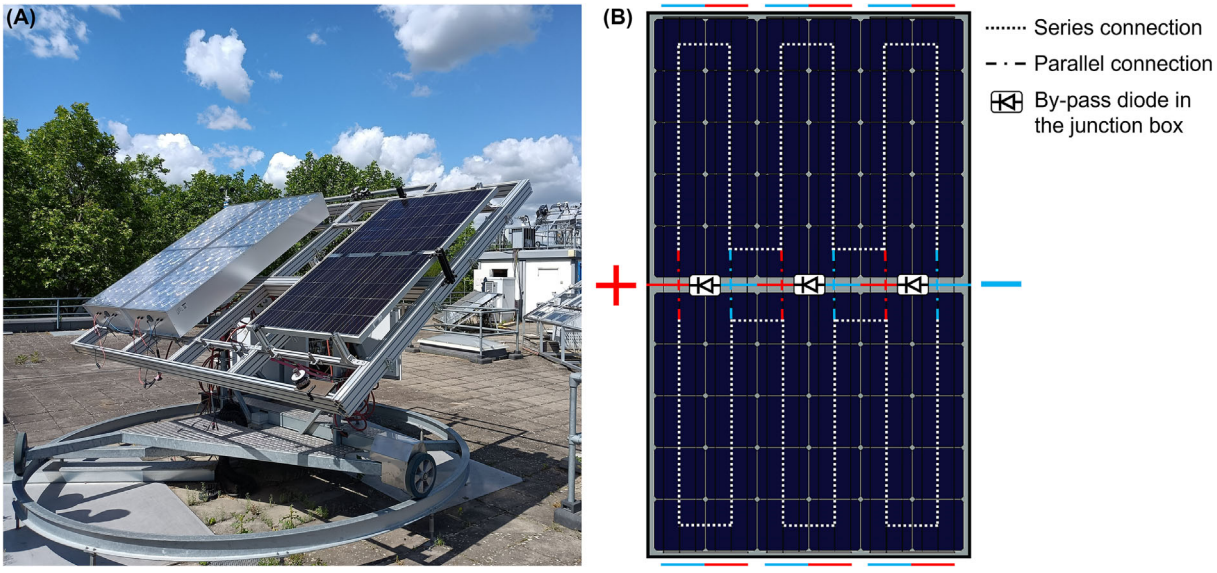

FIGURE 1 (A) Full-size bifacial Pero/Si tandem module mounted on the right side of the utilized dual axis tracker. Measurements were carried out with the outdoor measurement setup of Fraunhofer ISE CalLab located in Freiburg, Germany, 48.01° N, 7.83° E. (B) Schematic representation of the module's interconnection principle.

qualitative investigations as will be shown in the following section. Nevertheless, the values provided by the bottom cell (SMR13 and SMR23) should be considered especially when carrying out measurements for outdoor ratings since the effect of PW is mainly affecting the solar spectrum at wavelengths above 900 nm.[30,32] This is outside the sensitivity range of the middle cell sensor but still within the sensitivity range of the silicon bottom cells.

In contrast to CPV applications, the global normal irradiance (GNI) and not solely the direct component of the irradiated spectrum (DNI) can be converted into electrical energy and is consequently the relevant measurand for the investigation of flat-plate modules. Therefore, the component cells are not placed behind a collimator tube (as done for CPV applications[23,30,31]), but in a glass-covered housing, similar to a flat-plate module, making them exposed to the same portion of the sky as the module to be measured. Using these adapted component cells for the assessment of the outdoor spectral conditions, a "g" for global is added to the respective SMR values which is calculated for Cells 1 and 2, used throughout this publication, according to Equation (1).[25,30,33]

$$\mathrm{SMR12g} = \frac{I_{j_1}^{\mathrm{Meas}}}{I_{j_2}^{\mathrm{Meas}}} \cdot \frac{I_{j_2}^{\mathrm{Ref}}}{I_{j_1}^{\mathrm{Ref}}}. \quad (1)$$

$I_{j_1}^{\mathrm{Meas}}$ and $I_{j_2}^{\mathrm{Meas}}$ represent the short-circuit currents of the Component Cells 1 and 2 measured under the actual spectral conditions while $I_{j_1}^{\mathrm{Ref}}$ and $I_{j_2}^{\mathrm{Ref}}$ correspond to the short-circuit currents of both cells under AM1.5g[34] reference conditions. If SMR12g equals "one," the current balancing of both cells is equal to the balancing present if the cells are exposed to the reference spectral conditions. SMR12g values lower than "one" correspond to a red-shifted spectrum while values higher than "one" appear if the actual spectrum is blue-shifted compared to the spectral distribution of the AM1.5g reference spectrum. A photo of all three component cells is shown in Figure 2.

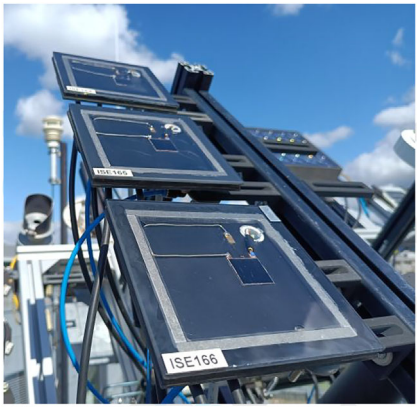

FIGURE 2 Component cell sensor (ISE164, ISE165, and ISE166) adapted from CPV applications for the evaluation of the spectral conditions during outdoor measurements of flat-plate modules.[25]

3.1 | Applicability for Pero/Si tandem measurements

As explained in the last section, SMR values equal to "one" indicate that the actual spectral conditions are resulting in the same subcell current ratio as the AM1.5g reference spectrum would. To investigate the applicability of the utilized component cell sensor for Pero/Si tandem measurements, we investigate whether SMR values close to unity can also indicate an AM1.5g like current balancing in the sample tandem module. Therefore, we are comparing the current ratios resulting for the component cell sensor (initially designed for CPV applications) and for the subcells of a Pero/Si tandem module under 519 spectra measured between April and June 2022 at our outdoor measurement setup in Freiburg, Germany. In Figure 3A, the normalized EQEs of the component cells (open symbols) and the normalized EQEs of a Pero/Si mini module (closed symbols), which is comparable to the full-size module investigated in this publication, are plotted. Additionally, the AM1.5g reference spectrum is shown on the right *y* axis. For the following comparison of the current matching ratios calculated based on the presented EQEs and the outdoor spectra, only Cells 1 and 2 are considered due to the reasons explained in the previous section. Figure 3B shows the $\mathrm{SMR}_{\mathrm{PSC/Si}}$ values calculated with the EQEs of the Pero/Si tandem device on the *x* axis as well as the respective SMR12g values calculated based on the component cell EQEs on the *y* axis. The relative deviation between both values calculated for each spectrum is shown on the right *y* axis. Comparing a linear fit ($R^2 = 0.994$, slope $= 1.009$, *y* intercept $= -0.015$) through the resulting datapoints (solid line) with the line of origin (dotted line), representing a perfect match between the axes, clearly shows a good agreement between both SMR values.

The reason for this high agreement can be explained by the fact that changes in AM and AOD are resulting in similar relative changes for both SMR values calculated with the sensor and device EQEs. Additionally, the solar spectrum is rather continuous within the investigated wavelength range and does not contain sharp peaks. Anyhow, this is usually not the case for solar simulator spectra which might lead to a completely different result for the comparison of the sensor and subcell characteristic shown above. According to this investigation, the maximum error introduced by using the presented unmatched component cell sensor for the evaluation of the outdoor spectral conditions the specimen module is exposed to is well below 2%. This result underlines the applicability of the utilized component cell sensor for the investigation of the outdoor performance of Pero/Si tandem modules presented in this publication. Nevertheless, we want to mention that for future outdoor ratings of Pero/Si or other flat-plate tandem devices also the SMR23g and SMR13g values, provided by the Component Cells 1 and 3 and 2 and 3, respectively, must be considered for the evaluation of the measurement data. Since the silicon bottom cell is affected by the amount of PW in the atmosphere, only the utilization of all three component cells can provide a universally valid evaluation of the outdoor spectral conditions, decrease measurement uncertainties, and therefore provide suitable evaluations for rating purposes which, however, are beyond the scope of this publication.

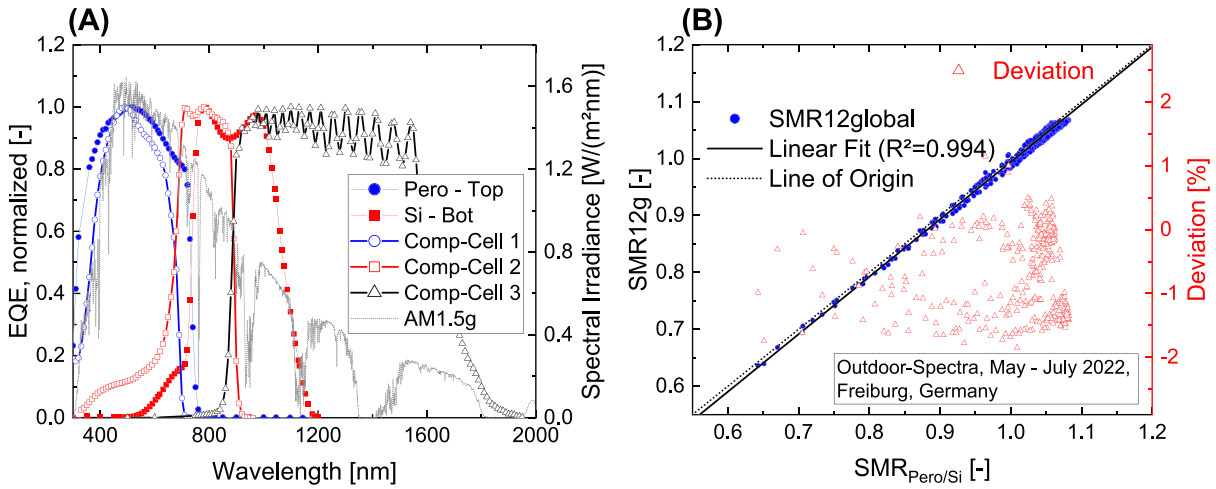

FIGURE 3 (A) Normalized EQEs of a Pero/Si tandem cell mono-module (closed symbols) and the component cells used for the evaluation of the outdoor spectral conditions (open symbols). All EQEs are normalized. The AM1.5g reference spectrum (dotted line) is plotted in the background. (B) Comparison of the SMR values calculated with the EQEs of the Pero/Si tandem device and respectively with the EQEs of the component cells for 519 outdoor spectra measured between April and June 2022. The line of origin defines an ideal match of the SMR values calculated with the different EQEs while the relative deviations between each corresponding SMR pair are plotted on the right *y* axis. The deviations shown are calculated by dividing the SMR12g values by the $SMR_{Pero/Si}$ values such that a positive deviation indicates the SMR12g value to be higher than the $SMR_{Pero/Si}$ value.

3.2 | Evaluation of ambient conditions

To facilitate the interpretation of the measurements shown in the following sections, the changes in the incident frontside irradiance throughout the measurement day are shown in Figure 4. The filled circles corresponding to the left *y* axis are showing the SMR12g values in dependence of the daytime plotted on the *x* axis. Starting from a very red-rich spectrum (SMR12g ~ 0.6) in the early morning the spectral conditions are changing to a more blue-rich distribution until the reference spectral conditions (SMR12g ~ 1.0) are reached at around 10:20 a.m. At SMR12g values close to "one," only small changes in the incident spectrum are visible for around 4 h. In the afternoon, the conditions are shifting back to a more red-rich spectral distribution. The black triangles, corresponding to the right *y* axis, are showing the GNI values measured throughout the investigated measurement day. To improve readability, only every fourth datapoint measured is plotted in this graph.

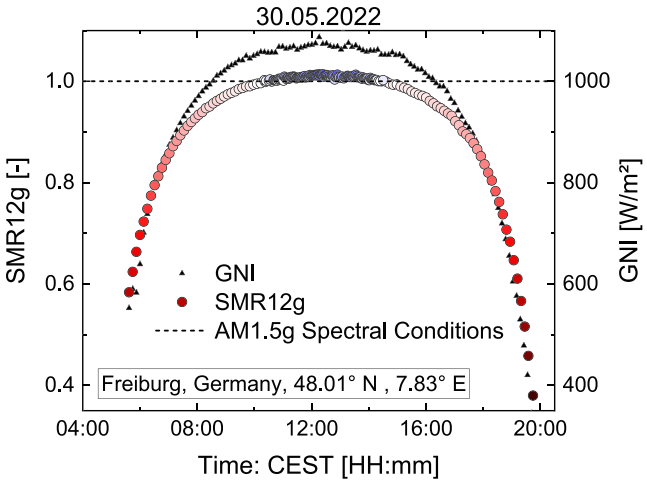

FIGURE 4 SMR12g values and GNI measured on the utilized dual axis tracker during the measurement day in Freiburg, Germany.

4 | INVESTIGATION OF THE MODULE'S CHARACTERISTIC

In the following, the measured *I*–*V* parameters are investigated individually to explain the module's characteristic under different measurement conditions. Based on the presented results, we explain the interplay of tandem and bifaciality effects affecting the individual *I*–*V* parameters in different ways. Doing this, we provide a deeper understanding of how measurements on bifacial Pero/Si tandem modules are influenced by realistic outdoor measurement conditions. The complete set of measurement data has been filtered to exclude unrealistic measurements which can originate from unstable irradiance conditions. All filtering parameters applied are described in Appendix A.1 of this publication. The resulting graphs for I_{SC}/GNI, V_{OC}, and *FF* as well as the frontside irradiance and backside irradiance (BSI) measured throughout the day are shown in Figure 5. Each graph shows the respective parameter plotted versus the SMR12g value on the bottom *x* axis, representing the outdoor spectral conditions.

The top *x* axis shows the parameter *Z* which, as the SMR value, describes the spectrum incident on the investigated sample. It is more

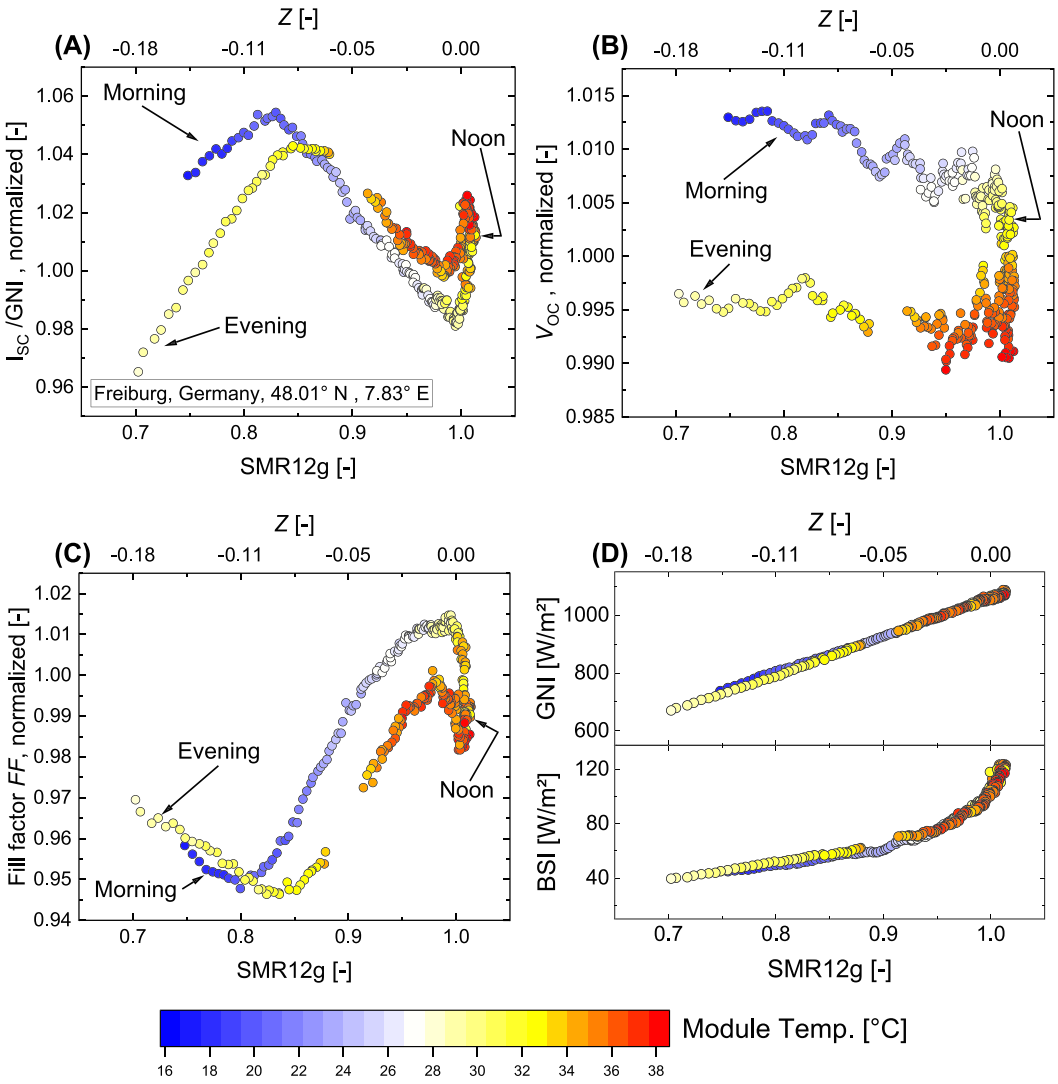

FIGURE 5 *I–V* parameters of the bifacial perovskite silicon tandem module measured outdoors in Freiburg, Germany. The color code used for all graphs is based on the module's temperature. The measurement data shown was filtered to exclude datapoints measured under unstable or otherwise distorted measurement conditions. This results in partially recognizable gaps in the course of the datapoints shown. (A) I_{SC} per GNI versus SMR12g, (B) V_{OC} versus SMR12g, (C) *FF* versus SMR12g, and (D) global normal and backside irradiance versus SMR12g.

commonly used in indoor characterizations of tandem devices[15,35] and serves as an additional reference for the measurements presented in this publication. Using this notation for outdoor measurements, the spectrum is defined by the ratio of short-circuit current generated in each component cell compared to its short-circuit current generated under the reference spectrum. As shown in Equation (2), this ratio can be represented by the factor *Z*, implying that the photocurrent of Cell 1 is $Z \cdot 100\%$ higher while at the same time the photocurrent of Cell 2 is $Z \cdot 100\%$ lower under the actual spectrum as it would be under reference spectral conditions.[15,35]

$$\frac{I_{j_1}^{Meas}}{I_{j_1}^{Ref}} = 1 + Z; \quad \frac{I_{j_2}^{Meas}}{I_{j_2}^{Ref}} = 1 - Z. \tag{2}$$

Using Equation (3), SMR12g can be converted into *Z*.

$$Z = \frac{SMR12g - 1}{SMR12g + 1}. \tag{3}$$

The color code used in the following graphs is based on the module's temperature, with the legend shown in the bottom of Figure 5. All parameters are normalized to their respective mean values measured under AM1.5g spectral conditions, defined by a SMR12g range of 0.995 to 1.005 for this publication.* The given range includes 60 datapoints measured between 10:00 a.m. and 14:50 p.m. Despite the normalization of the datapoints, qualitative information about the characteristic of the investigated bifacial tandem module, such as its performance under different spectral conditions, temperature effects

*For the considered datapoints, the SMR13g values range between 0.939 and 0.958 and the SMR23g values between 0.941 and 0.956.

on the individual subcells, and the influence of the BSI do not change due to the normalization of the measurements.

4.1 | Short-circuit current

Figure 5A shows the module's I_{SC} which was divided by the GNI plotted in Figure 5D. Plotting the I_{SC}/GNI instead of the I_{SC} itself enables the investigation of different parameters influencing the module's short-circuit current such as the spectral distribution, module temperature, and BSI, which would otherwise be hidden by the dominant influence of the change in GNI throughout the day as shown in Figure 4.

4.1.1 | SMR12g < 0.83—Morning

The first datapoint plotted was measured at 6:15 a.m. in the morning at a SMR12g value of 0.76 and a module temperature of 17.6°C (blue datapoint). Due to the red-rich spectral distribution in the early morning, the current of the overall module is limited by the perovskite top cells and is therefore increasing as the spectrum changes to more blue-rich conditions as the sun is rising. During the top cell current limitation, the rear-side irradiance has no effect on the module's overall short-circuit current since the photons reaching the module from the back are fully absorbed by the broadband silicon bottom cell.

4.1.2 | SMR12g ≈ 0.83—Morning

After the module's short-circuit current per GNI is rising due to the blue shift of the incident spectrum, a maximum is reached at a SMR12g value of 0.83. The maximum occurs due to the current match of both subcells. Note: For bifacial tandem modules, the current matching point[15] is affected by the frontside and rear-side irradiance onto the module, since the current generated in the silicon bottom cells results from the incident irradiance on both sides of the module.

4.1.3 | 0.83 < SMR12g ≤ 1.0—Noon

Due to the continuous blue shift of the frontside spectrum, the silicon bottom cells become current limiting. This results in a decrease in short-circuit current per GNI within the SMR12g range of 0.83 to 0.93. In contrast to the top cell-limiting condition, the rear-side irradiance does now fully contribute to the module's current, limited by the silicon bottom cells. The short-circuit current per GNI reaches a minimum at AM1.5g spectral conditions (SMR12g ~ 1). As shown in Figure 4, the spectral change is becoming lower during this time of the day such that the spectral distribution of the frontside spectrum remains relatively constant at a SMR12g value of "one." The BSI (Figure 5D) and the module temperature in contrast are significantly rising at the same time. Both effects are contributing to an increase of the silicon bottom cells' current. While the increasing BSI does obviously generate more charge carriers in the silicon bottom cells, the increasing temperature additionally contributes to this effect, resulting in a lower bandgap of the silicon bottom and a higher bandgap of the perovskite top cells.[16] Therefore, additional photons can contribute to the generation of current in the silicon subcells at both absorption edges. Due to the current limitation of the silicon bottom cells, the combination of both effects directly influences the short-circuit current of the overall module, which becomes visible in a strong increase of the short-circuit current per GNI at a SMR12g of approximately "one."

4.1.4 | 1.0 ≥ SMR12g > 0.85—Afternoon

After reaching a maximum at 12:16 a.m., the BSI decreases again in the afternoon, leading to a decrease in the module's short-circuit current per GNI. The constantly increasing red portion of the spectral distribution in contrast causes an increase in short-circuit current per GNI, which becomes visible when following the orange datapoints from SMR12g = 0.98 to lower values. Comparing the measurements carried out under the same spectral conditions earlier at the same day (blue datapoints), a significant difference in temperature and short-circuit current per GNI is visible. While there is no significant difference between the morning and afternoon BSI within the considered SMR12g range of 0.91 to 0.98, the variation in short-circuit current per GNI can be attributed to the increased module temperature and the resulting decrease in the silicon bottom cells' and increase in the perovskite top cells' bandgaps.[16] The datapoints missing within the SMR12g range of 0.88 to 0.91 have been excluded due to a reflection which was hitting the module's backside at this time of the day resulting in disordered measurements showing unrealistic high short-circuit current per GNI values.

4.1.5 | 0.85 ≥ SMR12g—Afternoon

At a SMR12g of around 0.85, another maximum is reached, which again shows the current match of the module's subcells. Due to the temperature-induced current increase of the silicon bottom cells combined with the current decrease of the perovskite top cells, the current match appears at more blue-rich spectral conditions and at a lower short-circuit current per GNI value in the afternoon. The temperature-driven current decrease in the perovskite top cells is also visible when comparing the short-circuit currents per GNI measured within the SMR12g range of 0.7 and 0.85 in the morning and in the evening, which can be clearly identified based on the color code of the datapoints.

Besides the explained temperature effect, degradation or metastability of the perovskite top cells might also explain the decreased short-circuit current per GNI measured in the evening. Significant degradation on such short time scales can be excluded based on

further measurements over a 2-week period. However, metastability effects, probably reversing overnight, may add up to the short-circuit current decrease driven by the negative temperature coefficient of the perovskite top cells. However, a detailed analysis of possible metastabilities of the module and their influence on the measurement data is beyond the scope of this publication.

4.2 | Open-circuit voltage

Since GNI and BSI values are quite similar for measurements carried out at spectral conditions resulting in the same SMR12g values throughout the day, the differences in the module's V_{OC} visible in Figure 5b can mainly be attributed to temperature effects. Due to the negative V_{OC} temperature coefficient of the investigated module, the highest V_{OC} values appear in the early morning with low module temperatures. As the temperature increases during the day, a decrease in V_{OC} to around 99% of the AM1.5g mean value is visible, despite the rise of the incident irradiance. With decreasing module temperature in the evening, the V_{OC} slightly increases again (0.9 > SMR12g > 0.7). While module temperatures of around 30°C (bright yellow color) have been measured in the evening (0.7 < SMR12g < 0.9) and at noon (0.98 < SMR12g < 1.0), the resulting V_{OC} values differ by around 0.75%. This deviation can be explained by a significant difference in the irradiance (around 200 W/m^2) incident to the module during the compared time periods.

4.3 | Fill factor

Such as the I_{SC} also the module's *FF*, plotted in Figure 5C shows a strong dependence on the incident spectral conditions.

4.3.1 | SMR12g < 0.8—Morning

Starting with 97% of the mean *FF* value under AM1.5g spectral conditions (0.995 < SMR12g < 1.005) in the early morning, the *FF* decreases continuously while the spectrum turns bluer. This blue shift of the frontside spectrum results in additional current generated in the perovskite top cells. Since the perovskite top cells are current limiting under the given spectral conditions, the ongoing increase of the top cells' short-circuit currents finally results in a current match of the subcells which in turn reveals in a fill factor minimum at a SMR12g value of 0.8.[15] While for an idealized tandem solar cell module the minimum in *FF* appears at the same spectral conditions as the I_{SC} maximum, the shift visible in the presented data could be explained by the shunt resistance of the perovskite top cells[15] (*I*–*V* curves shown in Appendix A.2). The underestimation of the *FF* in the forward scan during top cell limitation can give another explanation for the described effect which has already been shown in a spectrometric characterization of a Pero/Si tandem solar cell by Bett et al.[35]

4.3.2 | 0.8 < SMR12g < 1.0—Morning

Due to the remaining blue shift of the spectrum, the module's *FF* increases as the current limitation of the silicon subcells does. Comparing the slopes of the perovskite and silicon limiting branches on the left and right hand side of the current match a steeper *FF* increase under bottom cell-limiting conditions is visible. This effect results from the higher *FF* of the silicon subcells compared to the perovskite top cells, visible in the *I*–*V* curves under different current limiting conditions shown in Appendix A.2.

4.3.3 | SMR12g ≥ 1.0

While the increase of temperature and BSI are contributing to a steep short-circuit current increase as the spectral conditions are approaching SMR12g equals "one" (compare graph a), the contrary effect is visible for the *FF*. Due to the increased current of the limiting silicon bottom cells and the decreased current of the perovskite top cells, the current mismatch between the subcells decreases, which in turn results in a decrease in *FF*.[15]

4.3.4 | 1.0 > SMR12g ≥ 0.85—Afternoon

The same explanation holds when comparing the *FF* values measured in the morning and in the evening within the SMR12g range of 0.85 and 0.98. As the higher module temperature in the afternoon results in an increase in the silicon subcells' and a decrease in the perovskite top cells' short-circuit current, the *FF* decreases due to the temperature-induced change in the subcells' current match under similar front- and BSI conditions.

4.3.5 | 0.84 ≥ SMR12g—Afternoon

After reaching another *FF* minimum at a SMR12g value of 0.84, the module's current is limited by the perovskite top cells again, resulting in a slight increase of the *FF* as the current mismatch increases with the increasing red shift of the frontside spectral conditions. The higher *FF* values measured in the evening can be attributed to temperature-induced changes in the subcell currents. While the short-circuit current of the perovskite top cells decreases with temperature, the silicon bottom cells' short-circuit current increases resulting in a stronger current mismatch and therefore a higher *FF* under similar spectral conditions when compared to the measurements taken in the morning.

5 | POWER GENERATION AND CHARACTERIZATION OF BIFACIAL TANDEM MODULES

In the last section of this publication, we want to present the power generation of the investigated module throughout the measurement

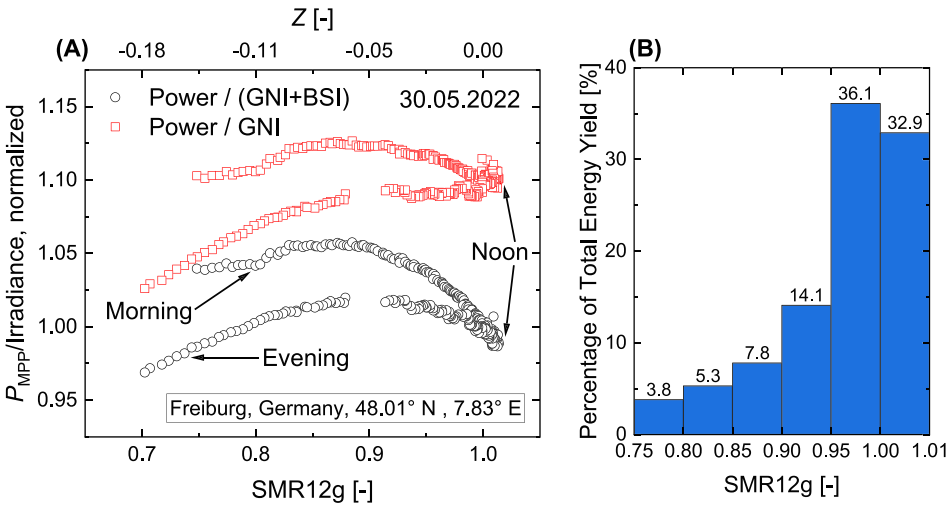

FIGURE 6 (A) Module power per irradiance calculated based on different irradiation definitions. Equivalent to the efficiency calculation, the datapoints shown as black circles have been calculated based on the sum of the frontside and rear-side irradiance. For the calculation of the red squares, on the other hand, only the frontside irradiance was considered. (B) Percentage share of total energy produced during the measurement day versus SMR12g. The measured datapoints have been binned on SMR12g steps of 0.05 and the mean power within these intervals has been calculated. Knowing the durations, the different SMR12g intervals appeared throughout the day the approximate energy productions have been calculated using the mean power measured within each interval.

day. Therefore, we will discuss the influence of the BSI and especially highlight how the combination of a tandem architecture and bifaciality affects a meaningful interpretation of the module's power generation potential.

The black circles in Figure 6A are showing the module's power per integral irradiance throughout the measurement day. For a bifacial module, the integral irradiance is the sum of GNI and BSI. As already mentioned for the investigation of the module's I_{SC}, presented in Figure 5A, the normalization on the irradiance is applied to enable the interpretation of the spectral dependence as well as the influence of the BSI on the output power. Looking at the resulting datapoints, one can see that the maximum power per irradiance doesn't appear at current matched conditions, as it would be expected for an "ideal" tandem device.[15] Instead, the maximum power output per irradiance is slightly shifted to more blue-rich spectral conditions (SMR12g = 0.88). This effect can be explained by the strong increase in *FF* (compare Figure 5C) which is overcompensating the reduced short-circuit current when shifting the module's operation out of the current match into bottom cell-limiting conditions.[35] The differences visible between the upper (morning) and lower (afternoon) curve of the black circled datapoints can be attributed to different module temperatures, where the decreased output power per irradiance is driven by the temperature-induced decrease in *FF* and V_{OC} discussed beforehand.[†] As the frontside spectral distribution becomes more blue-rich in the SMR12g range between 0.88 and 1.01, the output power per irradiance decreases.

However, for the evaluation of a bifacial module, solely focusing on the module's power per integral irradiance can lead to a misinterpretation of its actual yield potential. The datapoints discussed so far are calculated based on the sum of the frontside and rear-side irradiated power, which is following the approach of the efficiency definition.[37] In case of monofacial modules, however, only the frontside irradiance would be considered to determine the power per irradiance. A comparison of module efficiencies of monofacial and bifacial modules is therefore based on different irradiance definitions. Consequently, lower efficiencies result for bifacial modules due to the additionally considered BSI, provided that the module's rear-side efficiency is lower than its frontside efficiency.[38] The generated power per area, on the other hand, is expected to be higher for bifacial modules, due to the additional use of the BSI.[38] For the investigated module this becomes evident from the red squared datapoints, which show the module's power per frontside irradiance (GNI), providing more realistic values for a hypothetical comparison with a monofacial module with the same area. The influence of the BSI especially shows up at spectral conditions more blue-rich than the spectral conditions at the maximum power per GNI (0.88 < SMR12g < 1.01). Considering the black circled datapoints in the same spectral region the power per integral irradiance strongly drops due to the increased BSI which cannot be converted into output power as efficient as the frontside irradiance. Following the red squares instead the contribution of the BSI becomes visible, resulting in a relatively stable power output per GNI due to the additional contribution to the current generation in the silicon bottom cells which are limiting the current at the given spectral conditions. Based on the presented datapoints, one can see that, due to the discussed tandem and bifaciality effects, the module's power per GNI changes within a range of 10% (rel.) throughout

[†]The module has undergone the initial IEC61215[36] light stabilization procedures without relevant power change. This indicates at least a short-term light stability, and therefore, the power decrease visible in the evening is not expected to appear due to degradation of the module.

the measurement day. The minimum values appear in the early morning and evening, where the integral incident irradiance and therefore also the contribution to the energy yield is low as it can be seen in Figure 6B. In this graph, the approximate percentage share of the total energy production of the module during the measurement day versus SMR12g is shown. More than 90% of the energy is produced under spectral conditions resulting in SMR12g values higher than 0.85. The contributions arising under the very red-rich spectra in the early morning and late evening, which occur only for a short time and with a low integral irradiance, can therefore almost be neglected.

6 | SOURCES OF MEASUREMENT UNCERTAINTIES

Even though care has been taken to carry out measurements precisely, uncertainties are introduced due to the non-ideal measurement setup used for the presented first time measurement of a full-size Pero/Si tandem module at our outdoor measurement facility. As already mentioned, the presented *I*–*V* parameters are taken from forward *I*–*V* scans. Therefore, an error is introduced due to the difference between the forward and backward *I*–*V* curves of the investigated module. However, based on a comparison between forward and backward *I*–*V* curves with different subcell current limitation (shown in Appendix A.2), this error only affects the module's *FF* and P_{MPP}, since I_{SC} and V_{OC} are independent of the scan direction for the investigated module. Based on the individually measured *I*–*V* curves under strong perovskite limiting conditions the maximum error introduced to the measurement of the *FF* can be estimated to be around 3.3%, assuming the "real" *I*–*V* curve being equal to the reverse scan presented in Appendix A.2. The possible influence of this error for the *FF* evaluation has already been discussed for Figure 5C. As low hysteresis appears for measurements carried out under bottom cell-limiting conditions, the error discussed only affects 6.8% of the presented datapoints in the early morning and evening. Comparing the P_{MPP} values received from MPP tracking with the ones extracted from the *I*–*V* curves, we get mean deviations of 0.61% for silicon limiting and 1.03% for perovskite limiting measurement conditions. For the solely qualitative evaluation of the module's performance shown in this publication, these small uncertainties will be neglected. Another source of uncertainty is the measurement of the rear-side irradiance intensity carried out at only one position located at the upper end of the module, which probably results in an overestimation of the real BSI. Different albedos, different distances of the individual cells to the ground and shading by the tracker itself result in an inhomogeneous BSI distribution which cannot be quantified based on the measured sensor data. To overcome this problem, a higher number of rear-side irradiance sensors will be used for future measurements. The same situation appears for the measurement of the module's temperature, which does also not consider temperature inhomogeneities over the module area which can originate for example from wind hitting the module from only one side. Anyhow, the temperature cannot be measured on the back of each individual cell due to shading concerns, strongly affecting the bifaciality and therefore the module performance. Despite the discussed sources of uncertainties, which should serve for the correct classification of the presented data, we were able to present relevant and consistent conclusions of the qualitative characteristic of the investigated module, fulfilling the scope of this publication.

7 | CONCLUSION

We presented the first published outdoor measurement of a full-size Pero/Si tandem solar cell module investigating the influence of different outdoor measurement conditions on the module performance qualitatively. In the first part of this publication, we introduced the use of component cells, adapted for flat-plate module measurements,[25] to evaluate the outdoor spectral conditions based on their current ratios. The applicability of these component cells for measurements of Pero/Si tandem modules has been investigated based on outdoor spectra measured at our outdoor measurement facility between April and June 2022. Calculating the short-circuit current generated in the module's subcells as well as in the component cells, we were able to show that the resulting SMRs of the component cells fit the SMRs of the perovskite and silicon subcells under outdoor spectra with only small uncertainties. Therefore, we demonstrated the applicability of our measurement setup, for the reliable use with Pero/Si tandem solar cell modules.

After this preliminary investigation, we carried out *I*–*V* measurements on a full-size Pero/Si tandem module. For each single *I*–*V* curve, we evaluated the incident spectral conditions and the module temperature to accurately explain the characteristic of the module throughout a full measurement day. By combining the information of the frontside spectral distribution and intensity as well as the intensity of the rear-side irradiance, we were able to explain the interplay of both in real outdoor measurements.

While the frontside irradiance can be used by the perovskite and silicon subcells, the rear-side irradiance only contributes to the bottom cells' current. Therefore, the effect of a more red-rich frontside spectrum is equivalent to the effect of additional BSI. Based on this, it is obvious that the spectral distribution resulting in a current match of the subcells cannot be defined as clear as for monofacial tandem solar cell modules. Due to the dependence of current matching on the combination of frontside spectrum and incident rear intensity the current match conditions need to be investigated for each location individually making forecasts such as power yield calculations more complex. A higher BSI intensity would for example shift the position of the module's current match to more blue-rich and therefore closer to the reference spectral conditions. Consequently, the current match situation presented for the investigated module only represents an evaluation resulting from the BSI conditions appearing at this specific location and will vary for different locations and times of the year. However, the general effects and characteristic presented in this publication will not qualitatively change and must therefore be taken into account in the cell design.

We also evaluated the effect of temperature additionally affecting the subcells' current match, which is shifted to more blue-rich spectral conditions as the module temperature increases. Due to the different temperature coefficients of the perovskite top and silicon bottom cells, the module's temperature strongly affects all *I–V* parameters in an extensive way by virtue of its variable influence on the subcells' current balancing at different times of the day. To improve the performance of bifacial Pero/Si tandem solar cell modules under real world conditions, it is therefore important to take into account factors such as the influence of BSI intensity, the effect of the modules's operation temperature, and the interplay between these two factors, as described in this publication.

Discussing the module's power generation, we showed how the module's power per irradiance changes throughout the measurement day due to tandem and bifaciality effects. We highlighted that the maximum power output per irradiance of the investigated module does not appear at current matched conditions due to the overcompensation of the short-circuit current loss by a fill factor increase as the silicon bottom cells are becoming current limiting. We finally discussed how to accurately rate the influence of the BSI on the performance of a bifacial tandem solar cell module. This evaluation problem is solved for bifacial single-junction modules by specifying a back-surface "power gain,"[26] which in principle can be converted into a back-surface efficiency. However, this approach cannot be easily transferred for bifacial two-terminal tandem modules since the influence of the rear-side irradiance on the power output can't be regarded as a constant "gain factor" due to the series connection of the subcells. Instead, the backside contribution results from the actual current matching situation, which in turn depends on both the front-side and rear-side irradiance conditions as it has been presented and discussed in this publication. Therefore, new procedures and standards need to be developed to define how to deal with the influence of tandem effects on bifacial tandem modules to ensure a comparable and reliable assessment of these module's real-world performance.

ACKNOWLEDGEMENTS

This work was supported by the German Federal Ministry for Economic Affairs and Climate Action (BMWK) under contract number 03EE1087B (KATANA). The authors would like to thank Oxford PV for cooperation and the possibility to investigate the module presented in this publication. Open Access funding enabled and organized by Projekt DEAL.

CONFLICT OF INTEREST STATEMENT

The authors declare no conflict of interest.

DATA AVAILABILITY STATEMENT

Research data are not shared.

ORCID

David Chojniak https://orcid.org/0000-0001-9010-4468
Marc Steiner https://orcid.org/0000-0003-4870-9396
Sebastian Kasimir Reichmuth https://orcid.org/0000-0002-4963-0236
Stefan W. Glunz https://orcid.org/0000-0002-9877-2097

REFERENCES

1. Leijtens T, Bush KA, Prasanna R, McGehee MD. Opportunities and challenges for tandem solar cells using metal halide perovskite semiconductors. *Nat Energy*. 2018;3(10):828-838. doi:10.1038/s41560-018-0190-4
2. Heinrich M, Kuhn TE, Dimroth F, et al. A comparison of different solar cell technologies for integrated photovoltaics. In: *Proceedings of the 37th European Photovoltaic Solar Energy Conference and Exhibition*. WIP; 2020:1984-1994.
3. Philipps S, Warmuth W. Photovoltaics Report. Available at: https://www.ise.fraunhofer.de/de/veroeffentlichungen/studien/photovoltaics-report.html; 2022.
4. Li Z, Zhao Y, Wang X, et al. Cost analysis of perovskite tandem photovoltaics. *Joule*. 2018;2(8):1559-1572. doi:10.1016/j.joule.2018.05.001
5. Chouhan L, Ghimire S, Subrahmanyam C, Miyasaka T, Biju V. Synthesis, optoelectronic properties and applications of halide perovskites. *Chem Soc Rev*. 2020;49(10):2869-2885. doi:10.1039/c9cs00848a
6. Noh JH, Im SH, Heo JH, Mandal TN, Seok SI. Chemical management for colorful, efficient, and stable inorganic-organic hybrid nanostructured solar cells. *Nano Lett*. 2013;13(4):1764-1769. doi:10.1021/nl400349b
7. Bellini E. CSEM, EPFL achieve 31.25% efficiency for tandem perovskite-silicon solar cell. Available at: https://www.pv-magazine.com/2022/07/07/csem-epfl-achieve-31-25-efficiency-for-tandem-perovskite-silicon-solar-cell/; 2022.
8. Hutchins M. Oxford PV retakes tandem cell efficiency record. Available at: https://www.pv-magazine.com/2020/12/21/oxford-pv-retakes-tandem-cell-efficiency-record/; 2020.
9. Bellini E. Helmholtz Center achieves 29.80% efficiency for perovskite/silicon tandem solar cell; 2022.
10. Bellini E. KAUST claims 33.7% efficiency for perovskite/silicon tandem solar cell. Available at: https://www.pv-magazine.com/2023/05/30/kaust-claims-33-7-efficiency-for-perovskite-silicon-tandem-solar-cell/; 2023.
11. Ernst R. Researchers achieved world record 32.5% efficiency for a perovskite tandem solar cell. Available at: https://www.pv-magazine.com/2022/12/20/hzb-achieves-world-record-32-5-efficiency-for-perovskite-tandem-solar-cell/; 2022.
12. Li D, Zhang D, Lim K-S, et al. A review on scaling up perovskite solar cells. *Adv Funct Mater*. 2021;31(12):2008621. doi:10.1002/adfm.202008621
13. Oxford PV. Oxford PV sets new solar cell world record. Available at: https://www.oxfordpv.com/news/oxford-pv-sets-new-solar-cell-world-record; 2023.
14. International Electrotechnical Commission. *Photovoltaic Devices: Part 1-1: Measurement of Current-Voltage Characteristics of Multi-Junction Photovoltaic (PV) Devices*. 1st ed. 27.160(IEC 60904-1-1:2017). VDE Verlag; 2017.
15. Meusel M, Adelhelm R, Dimroth F, Bett AW, Warta W. Spectral mismatch correction and spectrometric characterization of monolithic III-V multi-junction solar cells. *Prog Photovolt: Res Appl*. 2002;10(4):243-255. doi:10.1002/pip.407
16. Aydin E, Allen TG, de Bastiani M, et al. Interplay between temperature and bandgap energies on the outdoor performance of perovskite/silicon tandem solar cells. *Nat Energy*. 2020;5(11):851-859. doi:10.1038/s41560-020-00687-4
17. Akhil S, Akash S, Pasha A, et al. Review on perovskite silicon tandem solar cells: status and prospects 2T, 3T and 4T for real world conditions. *Mater Des*. 2021;211:110138. doi:10.1016/j.matdes.2021.110138
18. Tillmann P, Jäger K, Karsenti A, Kreinin L, Becker C. Model-chain validation for estimating the energy yield of bifacial perovskite/silicon tandem solar cells. *Sol RRL*. 2022;6(9):2200079. doi:10.1002/solr.202200079

19. Jošt M, Lipovšek B, Glažar B, et al. Perovskite solar cells go outdoors: field testing and temperature effects on energy yield. *Adv Energy Mater*. 2020;10(25):2000454. doi:10.1002/aenm.202000454
20. de Bastiani M, van Kerschaver E, Jeangros Q, et al. Toward stable monolithic perovskite/silicon tandem photovoltaics: a six-month outdoor performance study in a hot and humid climate. *ACS Energy Lett*. 2021;6(8):2944-2951. doi:10.1021/acsenergylett.1c01018
21. Babics M, de Bastiani M, Balawi AH, et al. Unleashing the full power of perovskite/silicon tandem modules with solar trackers. *ACS Energy Lett*. 2022;7(5):1604-1610. doi:10.1021/acsenergylett.2c00442
22. Jaus J, Mißbach T, Philipps SP, Siefer G, Bett AW. Spectral measurements using component cells: examinations on measurement precision. In: *Proceedings of the 26th European Photovoltaic Solar Energy Conference*. WIP; 2011:176-182.
23. Peharz G, Siefer G, Araki K, Bett AW. Spectrometric outdoor characterization of CPV modules using isotype monitor cells. In: *Proceedings of the 33rd IEEE Photovoltaic Specialists Conference*. IEEE; 2008:1-5.
24. Siefer G, Bett AW. Calibration of III-V Concentrator Cells and Modules. In: *Proceedings of the 4th World Conference on Photovoltaic Energy Conference*. IEEE; 2008:745-748.
25. Steiner M, Siefer G. Translation of outdoor tandem PV module I–V measurements to a STC power rating. *Prog Photovolt: Res Appl*. 2023;31(8):862-869. doi:10.1002/pip.3691
26. International Electrotechnical Commission. *Photovoltaic Devices: Part 1-2: Measurement of Current-Voltage Characteristics of Bifacial Photovoltaic (PV) Devices*. 1st ed. 27.160(IEC TS 60904-1-2). VDE Verlag; 2019.
27. Klasen N, Lux F, Weber J, Roessler T, Kraft A. A comprehensive study of module layouts for silicon solar cells under partial shading. *IEEE J Photovolt*. 2022;12(2):546-556. doi:10.1109/JPHOTOV.2022.3144635
28. ET Instrumente GmbH. Electronic load ESL-solar: electronic load for test and characteristic of crystalline and thin film solar modules and cells. Available at: https://et-instrumente.de/index.php/en/products2/overview-electronic-loads/pv-modul-test-unit
29. Elumalai NK, Uddin A. Hysteresis in organic-inorganic hybrid perovskite solar cells. *Solar Energy Mater Solar Cells*. 2016;157:476-509. doi:10.1016/j.solmat.2016.06.025
30. Núñez R, Domínguez C, Askins S, et al. Determination of spectral variations by means of component cells useful for CPV rating and design. *Prog Photovolt: Res Appl*. 2016;24(5):663-679. doi:10.1002/pip.2715
31. International Electrotechnical Commission. *Photovoltaic Concentrators (CPV)—Performance Testing—Part 3: Performance Measurements and Power Rating*. 1st ed; ICS 27.160(IEC 62670-3:2017). VDE Verlag; 2017.
32. Stark C, Theristis M. The impact of atmospheric parameters on the spectral performance of multiple photovoltaic technologies. In: *2015 IEEE 42nd Photovoltaic Specialist Conference (PVSC)*. IEEE; 2015:1-5.
33. Domínguez C, Antón I, Sala G, Askins S. Current-matching estimation for multijunction cells within a CPV module by means of component cells. *Prog Photovolt: Res Appl*. 2013;21(7):1478-1488. doi:10.1002/pip.2227
34. International Electrotechnical Commission. *Photovoltaic Devices: Part 3: Measurement Principles for Terrestrial Photovoltaic (PV) Solar Devices with Reference Spectral Irradiance Data*. 4th ed; 27.160(IEC 60904-3:2019). VDE Verlag; 2019.
35. Bett AJ, Chojniak D, Schachtner M, et al. Spectrometric characterization of monolithic perovskite/silicon tandem solar cells. *Sol RRL*. 2022;7(2):2200948. doi:10.1002/solr.202200948
36. International Electrotechnical Commission. *Crystalline Silicon Terrestrial Photovoltaic (PV) Modules—Design Qualification and Type Approval*. 2nd ed; ICS 27.160(IEC 61215:2005). VDE Verlag; 2005.
37. International Electrotechnical Commission. *Solar Photovoltaic Energy Systems: Terms, Definitions and Symbols*. 3rd ed; ICS 27.160(IEC TS 61836:2016-12). VDE Verlag; 2016.
38. Kopecek R, Libal J. Bifacial photovoltaics 2021: status, opportunities and challenges. *Energies*. 2021;14(8):2076. doi:10.3390/en14082076
39. Bardizza G, Müllejans H, Pavanello D, Dunlop ED. Metastability in performance measurements of perovskite PV devices: a systematic approach. *J Phys Energy*. 2021;3(2):021001. doi:10.1088/2515-7655/abd678

How to cite this article: Chojniak D, Steiner M, Reichmuth SK, et al. Outdoor measurements of a full-size bifacial Pero/Si tandem module under different spectral conditions. *Prog Photovolt Res Appl*. 2024;32(4):219-231. doi:10.1002/pip.3753

APPENDIX A

Additional information to improve the traceability of the presented data and interpretations are given in the appendix.

A.1 | Filtering parameters

Measured datapoints are excluded from the evaluation if one of the following conditions is met:

- DNI/GNI < 0.6
- $I_{MPP}/I_{SC} > 1.0$
- $V_{MPP}/V_{OC} > 1.0$
- SMR12g > 2.0
- $\left|\left(1-\frac{GNI_{\text{before } I-V \text{ scan}}}{GNI_{\text{after } I-V \text{ scan}}}\right)\right| \cdot 100 > 1.0\%$
- BSI < 0 W/m^2 or BSI > 500 W/m^2
- Module temperature <0°C or module temperature >100°C
- Sun pointing error azimuth (x) > 0.5°
- Sun pointing error elevation (y) > 0.5°
- $\sqrt{x^2+y^2} > 0.5°$
- Time after sunrise (GNI > 500 W/m^2) < 45 min (applied to exclude measurements which might be disturbed due to light soaking effects[39]).

A.2 | Hysteresis in *I–V* curves

To quantify the hysteresis of the investigated tandem module and therefore estimate the error introduced by solely relying on the *I–V* parameter of the forward scan in the results section, individual forward and backward *I–V* curves have been measured with different subcell current limitations. The *I–V* curves presented in Figure A1A were measured under very red-rich spectral conditions in the early morning, resulting in a current limitation of the perovskite top cells. For this limitation condition, the hysteresis in P_{MPP} between the forward and backward *I–V* curves can be quantified to 3.2%, while I_{SC} (hysteresis below 0.15%) and V_{OC} (hysteresis ~0%) are not significantly influenced by the sweep direction. Figure A1B shows forward

and backward *I*–*V* curves under more blue-rich spectral conditions, resulting in a current limitation of the silicon solar cells, respectively. Since the *I*–*V* curves are primarily determined by the silicon bottom cells under these spectral conditions,[35] the hysteresis in P_{MPP} reduces to 0.4% and can therefore be neglected.

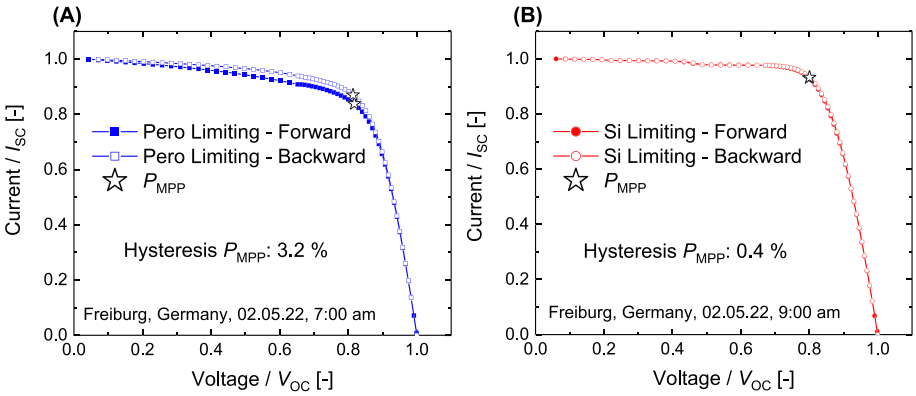

FIGURE A1 *I*–*V* curves measured in forward and backward sweep direction under different spectral conditions. (A) *I*–*V* curve measured while the perovskite top cells limit the overall current of the module. Due to the limitation conditions the perovskite solar cells mainly influences the shape of the module *I*–*V* curve resulting in a hysteresis at the P_{MPP} of 3.2%. I_{SC} and V_{OC} values are not affected by the hysteresis. (B) *I*–*V* curve measured while the silicon bottom cells limit the module's current. For the measurements carried out under silicon limitation, the hysteresis reduces to 0.4% and is therefore not relevant for the investigations carried out in this work.